PHYSICAL REVIEW APPLIED **1,** 024003 (2014)

Effect of Contacts in Organic Bulk Heterojunction Solar Cells

Oskar J. Sandberg,[*] Mathias Nyman, and Ronald Österbacka
Department of Natural Sciences, Center for Functional Materials, Åbo Akademi University,
Porthaninkatu 3, 20500, Turku, Finland

(Received 22 January 2014; revised manuscript received 7 March 2014; published 27 March 2014)

Interfaces play an important role in emerging organic electronic applications. In order to optimize and control the performance in organic devices such as organic solar cells, a comprehensive understanding of the contacts is essential. However, despite the vast progress made, a fundamental theory of the physical processes taking place at the contacts is still lacking. In this work, a numerical device model is used to clarify the effect of imperfect contacts in organic bulk heterojunction solar cells. The effect of increased injection barriers, reduced surface recombination, interfacial minority carrier doping, and traps for majority carriers at the electrodes causing reduced efficiencies is simulated. Two distinctly different underlying mechanisms leading to different S-shaped features are found, both leading to an effective shift of the built-in voltage. In the case of an extraction barrier to majority carriers at the contact, such as reduced surface recombination, the S kink is due to an induced diffusion potential. In the case of interfacial doping or traps, the S kink results from band bending caused by the fixed or trapped space charge. We derive analytical expressions describing the effective reduction of the built-in voltage and the (effective) open-circuit voltage providing means to quantify and distinguish the mechanisms. We show how to experimentally differentiate between these effects and provide tools to extract the relevant physical parameters.

DOI: 10.1103/PhysRevApplied.1.024003

I. INTRODUCTION

Organic solar cells have recently reached power conversion efficiencies over 10% [1]. The main advantages are the potential for large-scale production of light-weight and flexible thin films using small amounts of material and low processing temperatures making roll-to-roll printing from solution on flexible substrates possible [2–4]. Furthermore, the properties of organic materials can be manipulated on the molecular level using organic chemistry [4]. However, in order to make organic photovoltaics a competitive way of producing energy, the stability and lifetimes of the solar cells need to be increased [5,6]. To achieve this, more insights about the degradation processes are needed. Furthermore, in order to improve the device performance using new materials, it is essential to understand the effect of imperfect contacts.

The bulk heterojunction (BHJ) solar cell consists of a blended donor-acceptor active layer, usually a polymer-fullerene, forming an interpenetrating network. To ensure efficient charge extraction, the active layer is sandwiched between a hole-collecting anode and an electron-collecting cathode. Ideally, photogenerated holes are driven to the anode and electrons to the cathode by a built-in voltage where they will be collected to the external circuit [3,7]. We will, consequently, refer to holes and electrons as majority carriers at the anode and cathode, respectively.

The device performance of a solar cell is directly associated with the current-voltage characteristics (JV curve) obtained under illumination, the key parameters being the open-circuit voltage (V_{oc}), the short-circuit current (J_{sc}), and the fill factor (FF). A reduced device performance caused by imperfect contacts is, thereby, directly linked with a reduction of one or more of these key parameters. Perhaps the most prominent feature of imperfect contacts in organic BHJ solar cells is the appearance of an S kink in the JV curves under illumination giving rise to a strongly reduced FF. Doping caused by oxygen exposure [5,8], diffusion and accumulation of organic impurities to an electrode interface [9], vertical phase segregation [10], energy barriers to extraction [11], reduced surface recombination for majority carriers [12], increased injection barriers [13,14], or poor quality of the interfacial layers between the electrode and the organic layers have been attributed as possible sources. Additionally, defects, surface dipoles, and traps at the electrode interfaces have been discussed [15–17].

Controlled doping of organic solar cells can experimentally be realized by introducing dopants into the active layer [18–20]. It has been shown, however, that also charged defects in the organic materials can give rise to (unintentional) doping of the active layer [21,22]. Charged species in the active layer can originate from oxygen, organic impurities, or metal atoms from the electrodes. In some cases, water and molecular oxygen have been found to diffuse into the active layer through grains and pinholes in the electrodes, respectively [5]. It is well known that

---

[*] osandber@abo.fi

polymer solar cells usually suffer from photo-oxidation in the presence of oxygen and/or water creating charged species in the active layer [5]. The presence of water and oxygen near the electrodes might, therefore, give rise to a doping profile close to the contacts under illumination.

Mateker *et al.* [9] observed S-shaped JV curves that developed over a time interval of a couple of months in solar cells consisting of a blend of high-molecular weight poly(di(2-ethylhexyloxy)benzo[1,2-b:4,5-b']dithiophene- co-octylthieno[3,4-c]pyrrole-4,6-dione) (PBDTTPD) and [6,6]-phenyl C61-butyric acid methyl ester (PCBM). The inflection points are located in the reverse bias, far from the observed V_{oc} in these devices. They attribute the S-shape features to be a consequence of diffusion of organic impurities accumulating at and possibly reacting with the cathode [9].

Flexible device models are vital in order to understand the electrical behavior in organic devices and be able to interpret experimental data. Furthermore, a deeper understanding of the underlying physics is essential in order to improve and develop new experimental methods. To accurately describe the microscopic processes involved, Monte Carlo simulations are preferred [23]. However, these models are usually computationally time consuming, and a large part of the flexibility is lost. Macroscopic models based on a drift-diffusion approach, although computationally cheap, still contain relevant physics and have been successfully used in the past to describe the electrical behavior of organic BHJ solar cells [24–29].

Drift-diffusion models have also proven useful for investigating various contact-related effects in organic bulk heterojunction solar cells [11,12,15–17,29–35]. Aided by macroscopic simulations, Wagenpfahl *et al.* [12,32] found significantly reduced surface recombination velocities for majority carriers as a possible source to S-shaped JV curves and attributed the resulting band bending from the accumulated majority carriers as the reason for the deformed characteristics. A reduced surface recombination can be caused by an insulating layer at the electrode formed by unintentional oxidation, or a blocking layer. S-shaped JV curves can also be produced by explicitly introducing energy barriers to extraction (of majority carriers), as extensively investigated both experimentally and numerically by Tress *et al.* [11,33,34]. Furthermore, S shapes can also be obtained by implementing a reduced mobility profile for majority carriers near the electrode [35]. The effect of bulk doping in organic solar cells has been previously investigated using drift-diffusion models by several groups [36–38]; however, to our knowledge, no one has explicitly examined the effect of minority carrier doping (holes at the cathode and/or electrons at the anode) in the vicinity of the electrodes by means of electrical simulations. Furthermore, analytical expressions of how to quantify and distinguish between different mechanisms leading to S-shaped currents in BHJ solar cells are lacking.

In this paper, various contact effects leading to S-shaped JV curves in BHJ solar cells are investigated and compared by means of numerical drift-diffusion modeling. The influence of a reduced surface recombination velocity for majority carriers, interfacial doping of minority carriers in the vicinity of the electrodes, as well as traps at the electrodes are simulated. The emphasis is on obtaining an understanding of the underlying physics of how these factors alter the driving force for charge extraction giving rise to S-shaped JV curves. Since the driving force in BHJ is ideally provided by the built-in voltage, the effect of increased injection barriers and the role of the built-in voltage is analyzed also to provide a baseline for the discussion. The open-circuit voltage is known to be limited by the electrode work functions and the built-in voltage for unoptimized contacts [3,39,40]. An unintentional reduction of the built-in voltage might, therefore, lead to a reduction of the open-circuit voltage. The exact dependence between the built-in voltage and the open-circuit voltage at room temperature is still under debate [3,39–41]. In this paper, however, an analytical approximation for the open-circuit voltage explaining the injection barrier dependence and the role of the built-in voltage are presented also. Note that the effect of reducing the surface recombination for minority carriers is not considered in this work.

II. THE MODEL

Charge transport in disordered organic semiconductors is usually described by hopping transport in a Gaussian density of states (DOS) [42]. However, such a distribution can effectively be divided into two sets of states: conductionlike shallow states where the transport resembles band transport and traplike deeper lying states [3,27]. The charge transport can, therefore, be described by drift and diffusion of charge carriers in the conductionlike states. However, using effective macroscopic carrier mobilities $\mu_{n(p)}$ instead, the drift-diffusion relations for the total electron density n in the LUMO (lowest unoccupied molecular orbital) DOS and the total hole density p in the HOMO (highest occupied molecular orbital) DOS can be used [43,44]. We note that to explicitly take the effect of hopping transport and morphology into account, other models, such as kinetic Monte Carlo or multiscale modeling, are preferred [23].

The active bulk heterojunction layer is assumed to behave like an effective (intrinsic) semiconductor, where the holes are transported in the donor phase and the electrons in the acceptor [24]. The anode and cathode interfaces are defined at $x = 0$ and $x = d$, respectively, where d is the active layer thickness. A schematic picture is shown in Fig. 1(a). The numerical device model solves the one-dimensional carrier continuity equations coupled to the drift-diffusion equations. For electrons (holes), the continuity equation reads

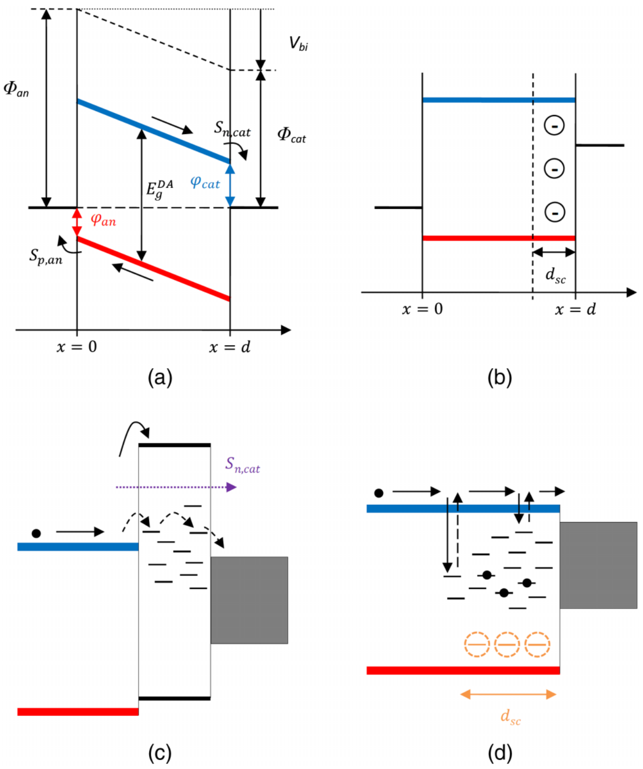

FIG. 1. Schematic of the energy diagrams in a BHJ solar cell. (a) Ideally, the majority carriers are driven to the respective electrode by a built-in voltage given by the electrode work function difference. The majority carrier injection barrier at the anode (holes) and the cathode (electrons) is given by φ_{an} and φ_{cat}, respectively. (b) The minority carrier doping is implemented by setting a fixed space charge in the vicinity of the electrode ranging a thickness d_{sc} into the active layer. (c) An extraction barrier, effectively described as a reduced surface recombination $S_{n,\mathrm{cat}}$, possibly created by an insulating oxide layer at the electrode. (d) A large density of (extrinsic) traps and/or charged species in a region near the electrode giving rise to a trapped or fixed space charge. As the trapping and release events slow down, the transport shallow traps can effectively be described by a reduced mobility. Note that if the density of gap states in (c) is large, transport via gap states in the insulating layer might become significant.

$$\underset{(-)}{+}\frac{1}{q}\frac{dJ_{n(p)}}{dx}+G_L-R=0, \tag{1}$$

with the current densities given by drift and diffusion as

$$J_n=q\mu_n nF+\mu_n kT\frac{dn}{dx}, \tag{2}$$

$$J_p=q\mu_p pF-\mu_p kT\frac{dp}{dx}. \tag{3}$$

Note that the Einstein relation $qD_{n(p)}=\mu_{n(p)}kT$ relating the diffusivity with the mobility is used in Eqs. (2) and (3) [45]. The carrier densities in a Gaussian DOS (using the Boltzmann approximation) are then expressed as [46]

$$n=N_c\exp\left(\frac{E_{Fn}-E_c}{kT}\right)\equiv N_c\exp\left(-\frac{qV_n}{kT}\right), \tag{4}$$

$$p=N_v\exp\left(\frac{E_v-E_{Fp}}{kT}\right)\equiv N_v\exp\left(-\frac{qV_p}{kT}\right), \tag{5}$$

where $N_{c(v)}$ is the effective density of states, and $E_{c(v)}$ corresponds to the LUMO (HOMO) levels shifted by $\sigma^2_{n(p)}/2kT$ into the gap from the center of the Gaussian DOS [$\sigma_{n(p)}$ is the width of the DOS].

The photogeneration rate of free charge carriers G_L is assumed to be constant throughout the active layer. The dominating recombination rate is assumed to be a bimolecular Langevin process

$$R=\beta(np-n_i^2), \tag{6}$$

with the bimolecular recombination coefficient given by $\beta=\frac{q}{\varepsilon\varepsilon_0}(\mu_p+\mu_n)$ and where $\beta n_i^2=\beta N_c N_v\exp\left(-\frac{E_g^{\mathrm{DA}}}{kT}\right)$ is the thermal generation rate (note that $G_L\gg\beta n_i^2$), and $E_g^{\mathrm{DA}}=E_c-E_v$ is taken as the effective band gap.

The space charge is related to the electric field F via the Poisson equation:

$$\frac{dF}{dx}=-\frac{q}{\varepsilon\varepsilon_0}(n-p+N_p-N_n+n_t-p_t), \tag{7}$$

where $N_{p(n)}$ is the concentration of $p(n)$ dopants and $p_t(n_t)$ is the density of holes (electrons) trapped in trap states originating from extrinsic sources (not LUMO or HOMO). Interfacial minority carrier doping in the vicinity of the cathode is realized by setting the doping concentration of holes N_p nonzero for $x>(d-d_{\mathrm{sc}})$, where d_{sc} is the thickness of the doped layer and zero otherwise [see Fig. 1(b)]. An analogous treatment is used to implement traps at the electrodes.

The total internal voltage over the active layer is given by

$$V-V_{\mathrm{bi}}=\int_0^d F dx, \tag{8}$$

where V is the applied voltage, and the built-in voltage is determined by the work function difference of the electrodes: $qV_{\mathrm{bi}}=\Phi_{\mathrm{an}}-\Phi_{\mathrm{cat}}$. The charge injection and extraction at the electrodes is described in terms of an effective surface recombination [12,15]. The electron current at the cathode reads

$$J_n(d)=-qS_{n,\mathrm{cat}}(n(d)-n_{\mathrm{cat}}), \tag{9}$$

where n_{cat} is the cathode electron density during thermal equilibrium, and $S_{n,\mathrm{cat}}$ is the electron surface recombination velocity at the cathode, effectively describing the electron transfer (hopping) rate between the electrode and the active organic layer surface. The injection barriers for the majority carriers are denoted by φ_{cat} and φ_{an} at the cathode and the anode, respectively, and defined as $qV_n|_{\mathrm{cat}} = \varphi_{\mathrm{cat}}$ and $qV_p|_{\mathrm{an}} = \varphi_{\mathrm{an}}$ [see Fig. 1(a)]. (For minority carriers, we have $qV_p|_{\mathrm{cat}} = E_g^{\mathrm{DA}} - \varphi_{\mathrm{cat}}$ and $qV_n|_{\mathrm{an}} = E_g^{\mathrm{DA}} - \varphi_{\mathrm{an}}$.) For an ideal contact, the surface recombination velocity is infinite [$n(d)$ reduces to n_{cat} in Eq. (9)]. In practice, a contact is considered ideal (for majority carrier extraction) if the charge extraction is limited by the charge transport in the active layer. If we assume that the bulk transport is drift dominated, the condition for an ideal contact is then $S \gg \mu F$. In this case, there is no extraction barrier present, and the charge injection is limited only by the thermionic injection barrier φ (the thermally activated carrier density at the contact) and not the charge-transfer rate. In contrast, if $S \ll \mu F$, both charge injection and extraction become contact limited. Here, we use the value $S = 10^6\ \mathrm{ms}^{-1}$ for an ideal contact. Note that in organic solar cells, the ideal case scenario is when $S = \infty$ for majority carriers (ideal extraction) and $S = 0$ for minority carriers (perfect blocking).

III. RESULTS AND DISCUSSION

The default parameters we use in the simulations are given in Table I. Unless otherwise stated, these parameters will be used. The mobilities are set equal to ease the analysis, and the generation rate of free carriers is set to correspond to a saturated net photocurrent density of $J_{\mathrm{ph,sat}} = qG_L d = 100\ \mathrm{Am}^{-2}$, where the thickness of the active layer is $d = 100$ nm. The undoped trap-free case with nonselective ideally extracting contacts ($S_{p,\mathrm{an}} = S_{p,\mathrm{cat}} = S_{n,\mathrm{an}} = S_{n,\mathrm{cat}} = 10^6\ \mathrm{ms}^{-1}$) is referred to as the ideal case in this paper. Unless otherwise stated, low injection barriers ($\varphi_{\mathrm{cat}} = \varphi_{\mathrm{an}} = 0.10$ eV) are assumed. In the simulations, starting from the ideal case, the cathode (or region near the cathode) is gradually degraded by either reducing the surface recombination velocity for electrons or introducing an adjacent layer with either a fixed negative space charge (p doping) or traps next to the contact. Note that since symmetric parameters are chosen, the case with degrading the anode instead is completely analogous.

TABLE I. Input parameters in the simulations. Unless otherwise stated, these parameters have been used in the simulations.

E_g^{DA}	1.2 eV
T	300 K
ε	3.4
d	100 nm
N_c, N_v	$10^{26}\ \mathrm{m}^{-3}$
μ_n, μ_p	$10^{-8}\ \mathrm{m}^2\ \mathrm{V}^{-1}\ \mathrm{s}^{-1}$
G_L	$6.24 \times 10^{27}\ \mathrm{m}^{-3}\ \mathrm{s}^{-1}$
φ_{cat}, φ_{an}	0.10 eV
$S_{p,\mathrm{an}}$, $S_{p,\mathrm{cat}}$, $S_{n,\mathrm{an}}$, $S_{n,\mathrm{cat}}$	$10^6\ \mathrm{ms}^{-1}$

A. Increased injection barriers

To provide a baseline for the discussion, we first investigate the effect of increased injection barriers on the open-circuit voltage in ideal devices. Note that an increase of the cathode (anode) injection barrier is equivalent to an increase (decrease) of the cathode (anode) work function (cf. Fig. 1). From Eqs. (4) and (5), the quasi-Fermi level difference between electrons and holes can be written as

$$E_{Fn} - E_{Fp} = E_g^{\mathrm{DA}} - qV_p - qV_n. \tag{10}$$

Since $\ln(np) \propto (E_{Fn} - E_{Fp})$, the maximum obtainable open-circuit voltage determined by the largest photogenerated quasi-Fermi level difference inside the active layer is given by

$$qV_{\mathrm{oc,max}} = E_g^{\mathrm{DA}} - \delta_p - \delta_n, \tag{11}$$

where $\delta_{n(p)} \equiv qV_{n(p)}|_{x=x_{\mathrm{max}}}$ with x_{max} corresponding to the point in the active layer where the product np is the largest.

At open-circuit conditions, the photogenerated charge carriers are canceled by recombination. If the dominating recombination mechanism is bimolecular, we have that $G_L \approx \beta(np - n_i^2)$ at x_{max}, and, consequently,

$$\delta_n = \frac{kT}{2}\ln\frac{\beta N_c^2}{G} + \frac{kT}{2}\ln\frac{p}{n}, \tag{12}$$

$$\delta_p = \frac{kT}{2}\ln\frac{\beta N_v^2}{G} + \frac{kT}{2}\ln\frac{n}{p}, \tag{13}$$

where $G = G_L + \beta n_i^2$. Direct insertion in Eq. (11) gives

$$qV_{\mathrm{oc,max}} = E_g^{\mathrm{DA}} - kT\ln\frac{\beta N_v N_c}{G}, \tag{14}$$

as expected for bimolecular recombination in case of low injection barriers [24,48,49].

For unoptimized contacts, however, the open-circuit voltage is known to be injection barrier dependent [39,40]. To understand this behavior, consider a device with ideal contacts. At open-circuit conditions, the output voltage determined by the quasi-Fermi level difference between the contacts is given by

$$qV_{\mathrm{oc}} = E_{Fn}|_{\mathrm{cat}} - E_{Fp}|_{\mathrm{an}}. \tag{15}$$

Utilizing the metal-insulator-metal concept, the following analytical expression explaining the injection barrier dependence is found for the open-circuit voltage (see Appendix A):

$$qV_{\mathrm{oc}} = E_g^{\mathrm{DA}} - \max(\varphi_{\mathrm{an}}, \delta_p) - \max(\varphi_{\mathrm{cat}}, \delta_n). \tag{16}$$

The derivation based on a drift-diffusion approach is presented in Appendix A. The relation between photogenerated carriers can be approximated as $\mu_n n_{ph} \approx \mu_p p_{ph}$ [47]. Using this approximation in Eq. (12) [Eq. (13)], one finds

$$\delta_{n(p)} \approx \frac{kT}{2} \ln \frac{\beta N_{c(v)}^2}{G} + \frac{kT}{2} \ln \frac{\mu_{n(p)}}{\mu_{p(n)}}. \tag{17}$$

This approximation is expected to break down at strongly imbalanced charge transport.

The simulated JV curves, both as a function of the applied voltage V and as a function of the total internal voltage $(V - V_{\mathrm{bi}})$, are shown in Fig. 2. Three different regimes for the open-circuit voltage as a function of the injection barriers are found, in complete agreement with Eq. (16). Note that δ_p and δ_n are both around 0.25 eV in Fig. 2. When both injection barriers are high, the open-circuit voltage is directly determined by the built-in voltage $(V_{\mathrm{oc}} = V_{\mathrm{bi}})$ given by the electrode work function difference, or, equivalently,

$$V_{\mathrm{bi}} = \frac{1}{q}(E_g^{\mathrm{DA}} - \varphi_{\mathrm{an}} - \varphi_{\mathrm{cat}}). \tag{18}$$

If, on the other hand, both injection barriers are low $[\varphi_{\mathrm{cat(an)}} < \delta_{n(p)}]$, the open-circuit voltage becomes independent of the injection barriers $(V_{\mathrm{oc}} < V_{\mathrm{bi}})$ and closely given by $V_{\mathrm{oc,max}}$ as per Eq. (14). The third scenario corresponding to the set of curves in the middle in Fig. 2(b) results when one of the injection barriers is high and the other is low. In this case, the open-circuit voltage depends only on the high injection barrier.

We stress that the influence of possible charge-transfer states [50], as well as the effect of disorder [51], are implicitly included in the effective band gap E_g^{DA} [49]. We further note that using the same approach as given above, it is straightforward to extend Eq. (17) to the case with purely trap-assisted recombination [28,49].

B. Reduced surface recombination for majority carriers

Simulated JV curves demonstrating the effect of reduced surface recombination velocities for electrons at the cathode are shown in Fig. 3(a). For comparison, also a JV curve for an ideal device but with an increased electron injection barrier is included and depicted by the thin dashed line. Interestingly, as long as only the working regime of the solar cell is considered $(V < V_{\mathrm{oc}})$, a sufficient reduction of the surface recombination velocity $S_{n,\mathrm{cat}}$ seems to be equivalent to effectively increasing the injection barrier φ_{cat} of an ideal device. In contrast to the case in Fig. 2, however, when the voltage is increased close to and above V_{oc}, the current remains relatively close to zero until the open-circuit voltage for the ideal device with low injection barrier is reached, resulting in an S shape. Note that a significantly reduced surface recombination for electrons at the cathode reduces both the extraction and injection of electrons at the cathode, leading to forward currents solely given by hole injection from the anode [12].

To relate the reduced surface recombination to an effective shift of the injection barrier, consider a BHJ solar cell having a reduced $S_{n,\mathrm{cat}}$. Neglecting space charge effects, the electric field is essentially zero at ideal flatband conditions and the transport is diffusion driven. Because of the (electron) blocking character of the cathode, the direction of the diffusion current will be towards the cathode (electrons diffuse towards the anode). Under these specific circumstances, the cathode current is given by $J_n(d) \approx \frac{qD_n}{L_n} n(d)$, where L_n is the diffusion length. According to Eq. (9), we can now rewrite

$$n(d) = n_{\mathrm{cat}} \exp\left(-\frac{\Delta_{S,\mathrm{cat}}}{kT}\right), \tag{19}$$

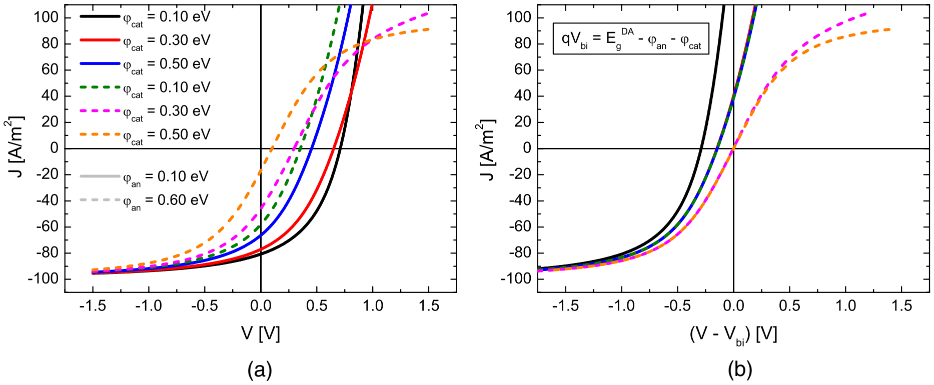

(a) (b)

FIG. 2. Simulated JV curves for an ideal BHJ solar cell under illumination for varying electron injection barriers φ_{cat} are displayed in (a). The solid lines correspond to a fixed hole injection barrier of $\varphi_{\mathrm{an}} = 0.10$ eV, while the dashed lines correspond to $\varphi_{\mathrm{an}} = 0.60$ eV. In (b), the simulated curves are rescaled as a function of the total internal voltage $(V - V_{\mathrm{bi}})$.

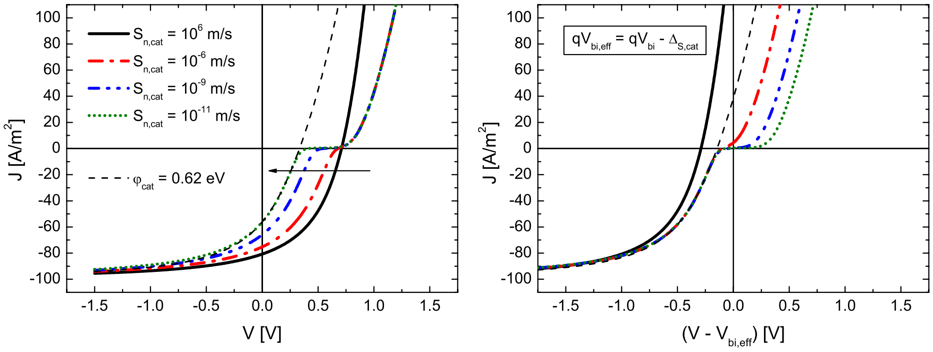

(a) (b)

FIG. 3. Simulated JV curves of a BHJ solar cell under illumination for varying surface recombination velocity $S_{n,\mathrm{cat}}$ at the cathode (colored lines). For comparison, also a JV curve with $S_{n,\mathrm{cat}} = 10^6\ \mathrm{ms}^{-1}$ but with an increased injection barrier $\varphi_{\mathrm{cat,eff}}$ given by the black dashed line is plotted in the figure. In (b), the simulated curves are rescaled as a function of an effective internal voltage $(V - V_{\mathrm{bi,eff}})$, with the corresponding effective built-in voltages given by $qV_{\mathrm{bi,eff}} = qV_{\mathrm{bi}} - \Delta_{S,\mathrm{cat}}$.

where $\Delta_{S,\mathrm{cat}} = kT \ln\left(1 + \frac{D_n}{S_{n,\mathrm{cat}} L_n}\right)$ is the effective shift of the built-in voltage induced by the increased diffusion potential formed by a reduced surface recombination of majority carriers. The effective shift $\Delta_{S,\mathrm{cat}}$ may also be interpreted as the effective extraction barrier that a reduced $S_{n,\mathrm{cat}}$ corresponds to. At open-circuit conditions (assuming the device is thin), the profiles for the charge carriers generated uniformly throughout the device are symmetric, and we approximate the diffusion length by $L_n = \frac{d}{2}$ [24]. Using $qD_n = \mu_n kT$, we obtain

$$\Delta_{S,\mathrm{cat}} = kT \ln\left(1 + \frac{2\mu_n kT}{qS_{n,\mathrm{cat}} d}\right). \tag{20}$$

The effective electron injection barrier during extraction conditions may then be written as

$$\varphi_{\mathrm{cat,eff}} = \varphi_{\mathrm{cat}} + \Delta_{S,\mathrm{cat}}, \tag{21}$$

where $\Delta_{S,\mathrm{cat}}$ is given by Eq. (20). Analogous expressions are valid for the case with a reduced hole surface recombination velocity at the anode. Indeed, the effective increase of the injection barrier required to fit the nonideal JV curves in Fig. 3(a) with the otherwise ideal device (thin dashed line) is closely given by Eq. (20).

In Fig. 3(b), the currents are rescaled as a function of $(V - V_{\mathrm{bi,eff}})$ with the effective built-in given by $qV_{\mathrm{bi,eff}} = qV_{\mathrm{bi}} - \Delta_{S,\mathrm{cat}}$. Given the crudity of the analytical model, a striking agreement is found between the numerical simulations and the analytical model [Eq. (21)] when $J < 0$. The influence of imbalanced mobilities is simulated in Fig. 4. A slight deviation between the nonideal curves and the ideal curves, with φ_{cat} effectively shifted by Eq. (20), starts to emerge in the reverse photocurrents of Fig. 4(a) when $\mu_n > \mu_p$. This deviation is explained by an increased bulk recombination of majority carriers in this case. Simulated JV curves with and without band bending (space charge effects) realized by setting $dF/dx = 0$ in the numerical model are shown in Fig. 5. As evident from Fig. 5, space charge effects and band bending *per se* are not needed to reproduce the S kink.

The effect of an extraction barrier, such as a reduced surface recombination velocity, for majority carriers is to decrease the effective driving force (built-in voltage) a

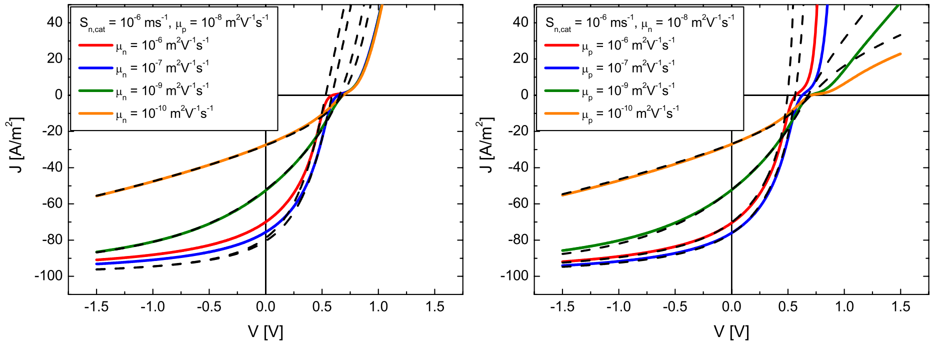

(a) (b)

FIG. 4. Simulated JV curves with imbalanced mobilities and a reduced surface recombination for electrons at the cathode for (a) varying electron mobilities and (b) varying hole mobilities. The thin dashed lines correspond to the respective ideal JV curves but with effectively increased electron injection barriers as per Eq. (21) in the main text.

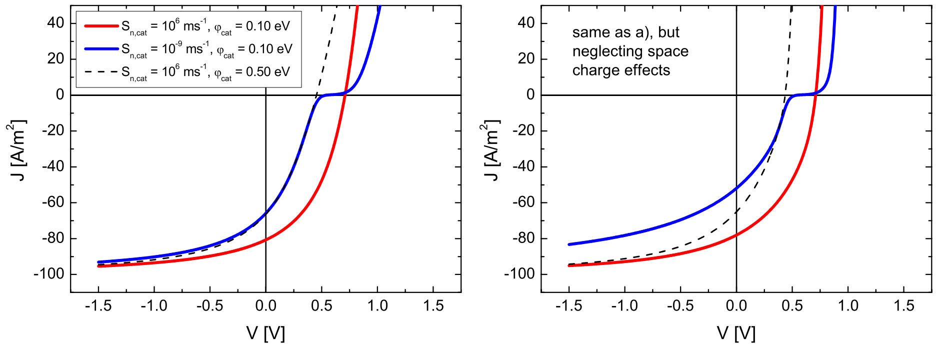

(a) (b)

FIG. 5. (a) Simulated JV curves with and without a reduced surface recombination for electrons at the cathode. The corresponding JV curves of an otherwise ideal device but with an effectively increased injection barrier as per Eq. (21) are included, depicted by the dashed lines. (b) Same as in (a) but neglecting band bending (space charge effects). [Note, however, that by neglecting band bending (counteracting the diffusion potential), a larger number of carriers is allowed to diffuse from the contacts increasing the recombination at short-circuit conditions.]

generated carrier experiences in the device during extraction conditions ($J < 0$). This reduction is seen as an effective increase of the injection barrier at the respective electrode. Based on the results above, we argue that the reduced FF in the S-shaped JV curves formed upon significantly reducing the surface recombination velocity is not due to space charge effects *per se* but rather a consequence of the induced diffusion potential (additional asymmetry) that an accumulation of charge carriers brings about.

C. Interfacial minority carrier doping in the vicinity of the electrodes

The case with a doped layer of holes adjacent to the cathode [see Fig. 1(b)] is simulated in Fig. 6. In Figs. 6(a) and 6(c), the effect of increasing thickness $d_{\rm sc}$ of the doped layer and concentration of dopants N_p on the JV curve is shown, respectively. In this case, a slightly different kind of S-shaped behavior is found, as compared to the case with reduced surface recombination velocities. Note that $d_{\rm sc} = d$ corresponds to the case when the entire active layer is doped (bulk doping).

For current densities below the open-circuit voltage ($V < V_{\rm oc}$), two different regions can be observed, provided that the doping concentration is high enough. At voltages close to $V_{\rm oc}$, the electric field is strongly screened by the space charge at the electrode, and the currents are strongly dominated by diffusion and recombination. Interestingly, the currents in this voltage region are identical to the case with same concentration of dopants but where the doping extends throughout the whole active layer. On applying a higher (negative) electric field, eventually an increase in the magnitude of the photocurrent (away from the bulk-doped case) is obtained, after which the current saturates to the ideally extracting case but with an effectively increased injection barrier. The S kink marks the transition between the behavior of a bulk-doped device and that of an undoped device.

To shed light on this behavior, consider a bulk-doped organic BHJ solar cell. If the doping is high enough ($N_p \gtrsim 3 \times 10^{22}$ m^{-3}), a negatively charged depletion region will form near the cathode, over which the total internal voltage ($V - V_{\rm bi}$) will drop [36,38]. Assuming a spatially constant doping concentration throughout the active layer, the thickness of the (abrupt) depletion region of fixed space charge is [52]

$$w = \sqrt{\frac{2\varepsilon\varepsilon_0(V_{\rm bi} - V)}{qN_p}}. \tag{22}$$

Note that since the electric field will be zero inside the neutral region $[0 < x < (d - w)]$, the current is dominated by diffusion in this region. Now consider the case with interfacial doping, where a thin layer $d_{\rm sc}$ at the cathode is p doped. As long as $w < d_{\rm sc}$, Eq. (22) is also valid in this case, since in both cases the total potential drop over the "neutral" region ($x \in [0, d - w]$) is zero, as evident from the simulated band diagrams in Fig. 7. When $V_{\rm bi} - V$ is increased to such an extent that $w = d_{\rm sc}$ is reached, the voltage drop over the depletion region is given by

$$\frac{\Delta_{p,\rm cat}}{q} = \frac{qN_p d_{\rm sc}^2}{2\varepsilon\varepsilon_0}, \tag{23}$$

where $\Delta_{p,\rm cat}$ is the magnitude of the band bending from the fixed space charge over the thickness $d_{\rm sc}$. However, since there are no dopants in the region $x \in [0, d - d_{\rm sc}]$, this corresponds to the point where the depletion region has reached its maximum value. By further increasing $V_{\rm bi} - V$, the additional potential difference now drops over the undoped region, increasing the electric field over the active layer. Consequently, the ideal (undoped) case has

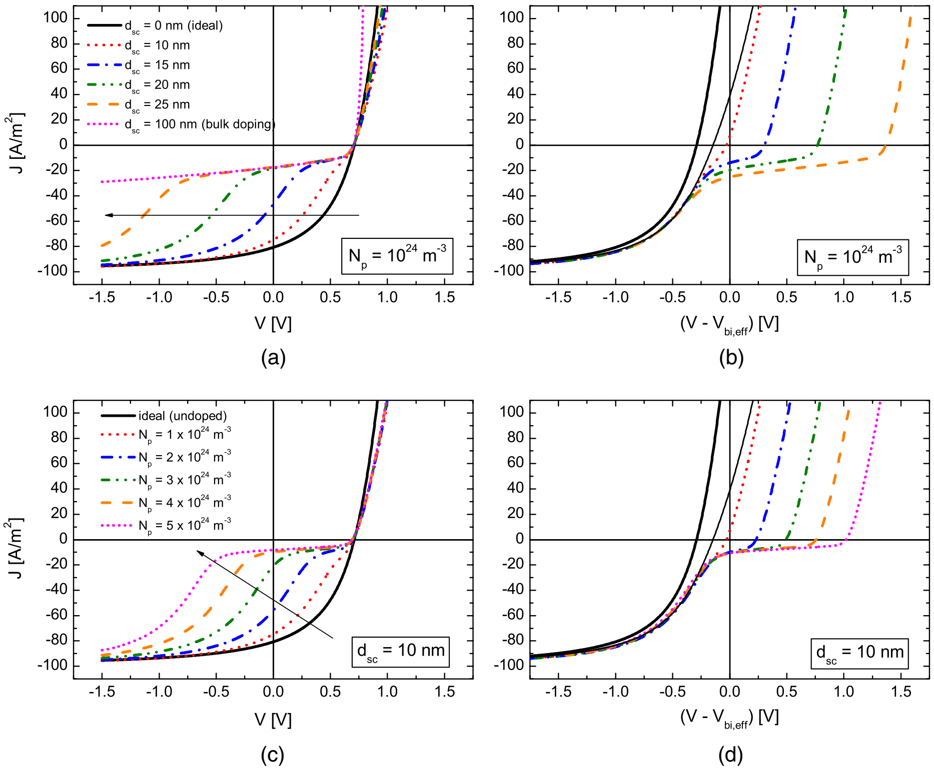

(a) (b)

(c) (d)

FIG. 6. Simulated JV curves for a BHJ solar cell under illumination for (a) varying thickness d_{sc} of the minority carrier doped layer at the electrode and (c) varying concentration of fixed minority carrier dopants. In (b) and (d), the curves from (a) and (c), respectively, are rescaled as a function of the effective internal voltage $(V - V_{\mathrm{bi,eff}})$, the effective built-in voltage given by $qV_{\mathrm{bi,eff}} = qV_{\mathrm{bi}} - \Delta_{p,\mathrm{cat}}$, where $\Delta_{p,\mathrm{cat}}$ is given in the text. The thin solid line represents the case for an ideal JV curve but with an effectively increased cathode injection barrier.

been regained but with the built-in voltage effectively replaced by

$$qV_{\mathrm{bi,eff}} = qV_{\mathrm{bi}} - \Delta_{p,\mathrm{cat}}, \tag{24}$$

where the band bending $\Delta_{p,\mathrm{cat}}$ given by Eq. (23) can be viewed as an effectively increased injection barrier: $\varphi_{\mathrm{cat,eff}} = \varphi_{\mathrm{cat}} + \Delta_{p,\mathrm{cat}}$. In Figs. 6(b) and 6(d), the curves from Figs. 6(a) and 6(c), respectively, are rescaled as a function of the effective internal voltage $V - V_{\mathrm{bi,eff}}$ over the (undoped) active layer, where $V_{\mathrm{bi,eff}}$ is given by Eq. (24). The thin black line corresponds to the ideal (undoped) case but with an effectively increased cathode injection barrier. Again, a striking agreement between the simulations and Eq. (24) is found within the undoped voltage region.

The behavior of minority carrier doping in the vicinity of the electrode is completely analogous to the case with reduced surface recombination velocities in terms of an effective built-in voltage. The mechanism leading to the S-shaped JV curves is, however, distinctly different for interfacial minority carrier doping. In this case, space charge effects and band bending at the interface are clearly important, and the S kink results from the transition between a region, where the field inside the bulk is strongly screened by the fixed space charge to a field-driven region

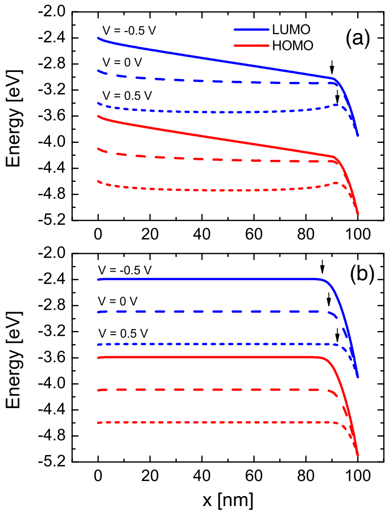

FIG. 7. Simulated band diagrams for cell under illumination at varying applied voltages for (a) p doping in the vicinity of the cathode ranging a thickness $d_{\mathrm{sc}} = 10$ nm into the active layer and (b) an entirely p-doped solar cell ($d_{\mathrm{sc}} = 100$ nm). The edge of the depletion layer of fixed space charge with the thickness w given by Eq. (22) is indicated with an arrow for the different applied voltages. The cathode is chosen as a reference electrode with the Fermi level at −4.0 eV.

where the depletion layer formed by the fixed space charge has reached the thickness of the doped region. The field-driven region corresponds to the ideal case but with the built-in voltage effectively reduced by the band bending from the fixed space charge.

D. Effect of traps for majority carriers at the electrode interfaces

The influence on JV characteristics of a large electron trap density near the cathode interface is simulated in Fig. 8. Single-level traps with a trapped electron density $n_t = N_t[1+\exp(\frac{E_{\mathrm{trap}}-E_{Fn}}{kT})]^{-1}$ and a trap depth of $E_t = E_c - E_{\mathrm{trap}}$, where N_t is the trap density and E_{trap} is the trap level, have been assumed. In Fig. 8(a), the trap depth is varied. In case of deep traps ($E_t = 0.5$ eV), the density of trapped electrons is $n_t \approx N_t$, effectively acting as a fixed space charge, and, thus, completely equivalent to the case with interfacial minority carrier doping. For shallow traps, however, the trap-filling effect becomes important. The space charge from the occupied shallow traps is, consequently, voltage dependent in this case, and a distinctly different S shape is found. In Fig. 8(b), JV curves for varying trap density N_t with $E_t = 0.3$ eV (shallow traps) are shown. Eventually, when a high enough reverse bias is applied and the trap-filled limit is entered, the ideal photocurrent behavior (with a built-in voltage effectively shifted by the band bending from the filled traps) is regained.

By instead reducing the majority carrier mobility μ_t near the electrode, as depicted in Fig. 8(c), a similar behavior as in Fig. 8(b) is found. This is because the effect of shallow traps can be incorporated in an effective mobility $\mu_t \approx \frac{n}{n_t}\mu$ [53]. The deviations between the curves in Figs. 8(b) and 8(c) (especially seen in the forward currents), mainly arise from the abrupt mobility difference at the interfaces of the low-mobility region creating additional barriers to extraction and injection in this case. We note that a reduced mobility near the electrode interface can also be used to effectively describe transport through gap states in an insulating layer at the electrode, e.g., formed by unintentional oxidation of the electrode [see Fig. 1(c)]. If the insulating layer has a high barrier to extraction but contains a large density of gap states, transport through gap states might become important.

The effect of deep traps for majority carriers at the electrode is equivalent to minority carrier doping in the vicinity of the electrodes, the sharp S-shaped JV curves being a direct consequence of the fixed trapped space charge at the electrodes. In case of shallow traps, the space charge is voltage dependent as the trap filling becomes important. Consequently, a prolonged S-shaped region is found. A similar S-shaped behavior is found between shallow traps for majority carriers and reduced majority carrier mobility profile near the electrode; however, an additional effective barrier to extraction is formed in the reduced mobility case.

E. How to experimentally distinguish between different contact-related mechanisms leading to S-shaped JV curves

The different mechanisms resulting in S-shaped JV curves presented above show distinctly different behaviors. When comparing a nonideal device to an ideal one, it is in some cases possible to determine the dominating underlying mechanism causing the S kink. The clarification and quantification of the underlying mechanisms will be easier and more reliable if an ideal JV curve is available as well as the nonideal. For example, when performing degradation studies or when replacing a metal contact with cheaper alternatives, an ideal device is often available. However, when developing new materials and device architectures, the ideal JV is not available, and in these cases, quantification of the relevant factors is difficult, but some conclusions can be drawn from the shape of the JV curves.

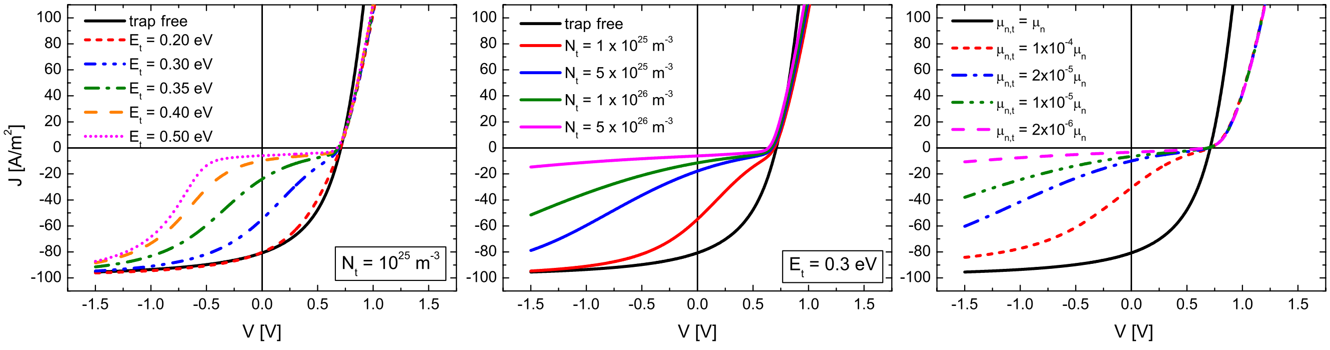

(a) (b) (c)

FIG. 8. Simulated JV curves having various densities of majority carrier traps near the electrode ranging $d_{\mathrm{sc}} = 7$ nm into the active layer from the electrode for (a) varying trap depth E_t and (b) varying trap density N_t with a trap depth of $E_t = 0.3$ eV corresponding to shallow traps. In (c), the trap-free case but instead with a reduced majority carrier mobility at the region ranging 7 nm into the active layer from the electrode is shown.

In order to do this, one should first look at the position of the inflection point (located near the green stars in Fig. 9). In the case of reduced surface recombination, the inflection point is positioned in the vicinity of the x axis. By shifting the nonideal JV curve so that it overlaps with the ideal one (in reverse bias), as shown in Figs. 9(a) and 9(b), the shift $\Delta V_{\mathrm{oc}}^{\mathrm{eff}}$ between the ideal $V_{\mathrm{oc}}^{\mathrm{ideal}}$ and the nonideal effective $V_{\mathrm{oc}}^{\mathrm{non,eff}}$ (green stars in Fig. 9) can be expressed as

$$q\Delta V_{\mathrm{oc}}^{\mathrm{eff}} = \Delta_{\mathrm{cat(an)}} + \varphi_{\mathrm{cat(an)}} - \max\left(\varphi_{\mathrm{cat(an)}}, \delta_{n(p)}\right), \quad (25)$$

where $\Delta_{\mathrm{cat(an)}}$ is the effective shift of the built-in voltage. In case of a reduced surface recombination for electrons (holes) at the cathode (anode), $\Delta_{\mathrm{cat(an)}} = \Delta_{S,\mathrm{cat(an)}}$. From Eq. (25), the effective shift $\Delta_{S,\mathrm{cat(an)}}$ of the built-in voltage and, thus, the reduction in the surface recombination velocity can be determined as per Eq. (20). Note that taking $N_c \approx N_v$, we may rewrite Eq. (17): $\delta_{n(p)} \approx \frac{1}{2}[E_g^{\mathrm{DA}} - qV_{\mathrm{oc,max}} - kT\ln(\frac{\mu_{n(p)}}{\mu_{p(n)}})]$, where $V_{\mathrm{oc,max}}$ is the open-circuit voltage of the ideal device with Ohmic (optimized) contacts. If the injection barrier $\varphi_{\mathrm{cat(an)}} > \delta_{n(p)}$, Eq. (25) reduces to $q\Delta V_{\mathrm{oc}}^{\mathrm{eff}} = \Delta_{\mathrm{cat(an)}}$.

If the ideal JV curve is not available, the distance between the two inflection points can be used as an approximate assay of the surface recombination velocity: the longer the distance between the inflection points, the lower the surface recombination velocity. This is a useful rule of thumb when comparing several nonideal JV curves. However, due to the exponential dependence on Δ_S, it is difficult to quantify the surface recombination velocity in this case.

In the case of deep traps (or doping) and shallow traps, the inflection point appears below the x axis (higher trap density moves the inflection point towards the x axis). The current at strong reverse bias corresponds to the undoped case, whereas close to the inflection point, the current corresponds to the case where the concentration of trapped or fixed space charge stretches through the whole of the bulk. The deeper the traps, the sharper this transition is. By shifting the ideal JV curve to overlap with the nonideal one, as shown in Figs. 9(c) and 9(d), the effectively shifted open-circuit voltage $V_{\mathrm{oc}}^{\mathrm{non,eff}}$ can be estimated and $\Delta V_{\mathrm{oc}}^{\mathrm{eff}}$ evaluated. Using Eq. (25), the effective shift of the built-in voltage that is caused by a fixed or trapped space charge density in the vicinity of the electrode can be determined. This shift is related to both the density and the thickness d_{sc} of the fixed space charge layer through Eq. (24). In principle, it should be possible to independently determine the density either by using Mott-Schottky analysis (within

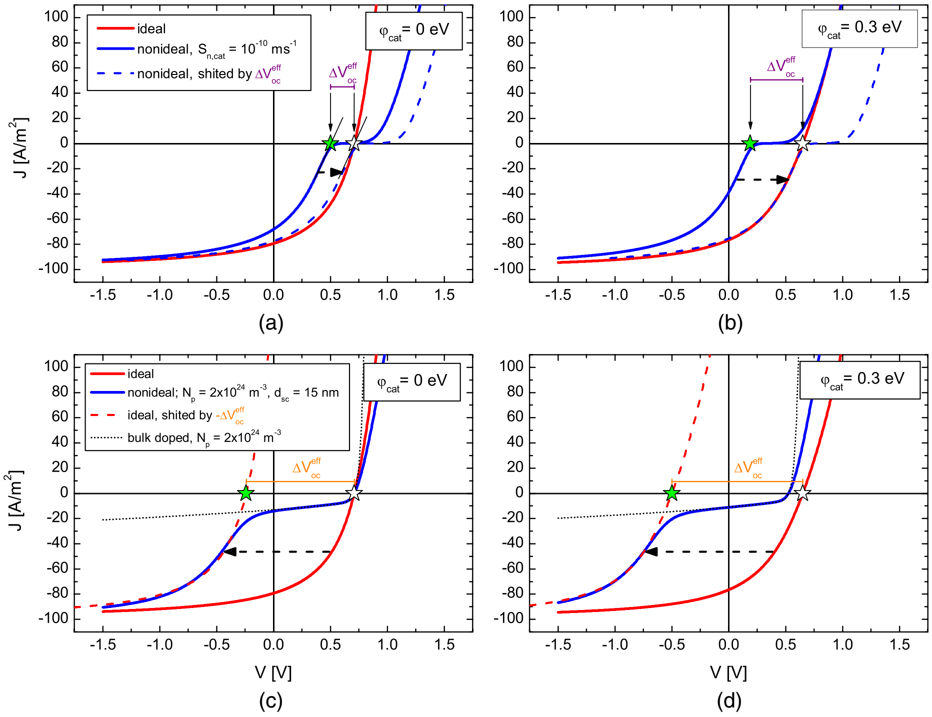

FIG. 9. Method to extract the relevant contact-related parameters from JV curves (see main text). The case with a reduced surface recombination illustrated in (a) and (b), while the case with interfacial doping at the cathode interface is given in (c) and (d). The effective V_{oc} shift between the ideal and the cell with a nonideal cathode is given by $q\Delta V_{\mathrm{oc}}^{\mathrm{eff}} = \Delta_{\mathrm{cat}} - \max(\delta_n, \varphi_{\mathrm{cat}}) + \varphi_{\mathrm{cat}}$. From the JV curves in (a) and (b), $\Delta V_{\mathrm{oc}}^{\mathrm{eff}}$ is found to be 0.20 and 0.45 V, respectively, leading to $\Delta_{S,\mathrm{cat}} \approx 0.45$ eV. Using Eq. (20), we find $S_{n,\mathrm{cat}} \approx 10^{-10}$ ms^{-1} (in accordance with the input value). In a similar fashion, $\Delta V_{\mathrm{oc}}^{\mathrm{eff}}$ is found to be around 0.95 and 1.2 V in (c) and (d), respectively, giving $\Delta_{p,\mathrm{cat}} \approx 1.2$ eV. Note that if the cathode injection barrier φ_{cat} is high, $qV_{\mathrm{oc}}^{\mathrm{eff}} = \Delta_{\mathrm{cat}}$.

the voltage range where the current is dominated by doping) [38], or charge extraction by linearly increasing voltage [54]. The current extrapolated from the inflection point towards reverse bias [the dotted (bulk-doping) line in Figs. 9(c) and 9(d)] corresponds to constant doping concentration. Note that if the ideal JV curve is not known in this case, the effective shift can be approximated by the distance between the two inflection points.

In the cases of shallow traps and/or reduced effective mobilities, the trap concentrations and mobilities are difficult to quantify. However, by observing the position of the inflection point and how quickly the reverse bias current saturates, one can draw some conclusions as to what is the dominating effect.

As a practical demonstration, this approach is applied to the experimental results reported by Mateker *et al.* [9], where it was observed that an S kink developed over time. The inflection point is located far in reverse bias, well below the x axis, which implies that the kink is due to doping near the interface, consistent with their explanation. The S-shaped JV curves reported by Lilliedal *et al.* [8] on inverted P3HT:PCBM cells containing electron-collecting layers of ZnO, on the other hand, seem qualitatively similar to the case with reduced mobility near the electrode. As the cells were stored and operated in ambient air, a mechanism based on the formation of oxygen radicals in ZnO was proposed as the underlying reason for the inflection points [5,8]. As negatively charged oxygen radicals are expected to slow down the electron transport in the ZnO layer, an effectively reduced electron mobility at the cathode is in agreement with the proposed mechanism.

IV. SUMMARY

We use a numerical device model to clarify the effect of imperfect contacts leading to S-shaped JV characteristics in bulk heterojunction solar cells. The effect of reduced surface recombination velocities, interfacial minority carrier doping, and traps for majority carriers at the electrodes are simulated and compared to the case with increased injection barriers. We find two different underlying mechanisms responsible for the S-shaped JV curves and are able to derive analytical expressions to distinguish and quantify between various contact-related mechanisms leading to S-shaped JV curves. Also, an analytical expression explaining the injection barrier dependence of the open-circuit voltage is derived.

The effect of reduced surface recombination velocities is shown to decrease the effective driving force (built-in voltage), a generated carrier experience in the device. This reduction is seen as an effective increase of the injection barrier at the respective electrode and is not due to space charge effects *per se* but rather a consequence of the induced diffusion potential (additional asymmetry) that an accumulation of charge carriers brings about. We provide means to calculate the reduction in the surface recombination velocity from actual measurement data.

The behavior in the case of minority carrier doping in the vicinity of the electrode is completely analogous in terms of an effective built-in voltage to the case with reduced surface recombination velocities. The underlying mechanism is, however, decidedly different. The S kink results from the transition between a region where the field inside the bulk is strongly screened by the fixed space charge, to a field-driven region where the band bending from the charged dopants reaches its maximum value effectively shifting the built-in voltage. If this transition is sharp, it is possible to estimate the doping concentration and the width of the doping layer according to the recipe given in Sec. III E.

The effect of traps at the electrodes is, in general, not easily quantifiable. The effect of deep traps for majority carriers at the electrode is equivalent to minority carrier doping in the vicinity of the electrodes; the trap density can, in this case, be calculated in the same way as the doping concentration. In the case of shallow traps, the space charge is voltage dependent, which results in a prolonged S shape and makes it difficult to quantify the trap density. Furthermore, the case of shallow traps is qualitatively similar to reduced effective mobilities in the vicinity of the contacts during extraction conditions.

In general, there might be several contact-related imperfections that give rise to S-shaped JVs, and in these cases, it is difficult to determine exactly all the mechanisms involved. However, the results we present here provide tools to determine the dominating effect and, in some cases, quantify the processes involved in the contact degradation.

ACKNOWLEDGMENTS

Partial financial support from the Academy of Finland through Projects No. 141115 and 135262 is acknowledged. O. J. S. acknowledges funding from the National Graduate School of Nanosciences (Nano-NGS) and R. Ö. a personal grant from The Swedish Cultural Foundation in Finland.

APPENDIX A: ANALYTICAL DERIVATION OF THE OPEN-CIRCUIT VOLTAGE

In this section, an analytical expression of the open-circuit voltage in bulk heterojunction solar cells assuming the metal-insulator-metal picture is derived. To understand the injection barrier dependence of the open-circuit voltage, consider a device with ideal contacts at open-circuit conditions. The output voltage is given by

$$qV_{\mathrm{oc}} = E_{Fn}|_{\mathrm{cat}} - E_{Fp}|_{\mathrm{an}}, \tag{A1}$$

where $E_{Fn(p)}|_{\mathrm{cat(an)}}$ is the electron (hole) quasi-Fermi levels at the cathode (anode). Denoting $\pm\Delta E_{Fn(p)} = E_{Fn(p)}|_{x=x_{\max}} - E_{Fn(p)}|_{\mathrm{cat(an)}}$ [where $x_{\max}$ is defined as in

Eq. (11)], and further using Eq. (11), the open-circuit voltage can be rewritten as

$$qV_{\mathrm{oc}} = qV_{\mathrm{oc,max}} - \Delta E_{Fn} - \Delta E_{Fp}. \tag{A2}$$

Using Eq. (10), noting that $qV_{n(p)}|_{x=x_{\mathrm{max}}} = \delta_{n(p)}$ and $qV_{n(p)}|_{\mathrm{cat(an)}} = \varphi_{\mathrm{cat(an)}}$, we rewrite ΔE_{Fn} and ΔE_{Fp} in Eq. (A2) as

$$\Delta E_{Fn} = \Delta E_c - \delta_n + \varphi_{\mathrm{cat}}, \tag{A3}$$

$$\Delta E_{Fp} = \Delta E_v - \delta_p + \varphi_{\mathrm{an}}, \tag{A4}$$

where $\Delta E_c = E_c|_{x_{\mathrm{max}}} - E_c|_{\mathrm{cat}}$ and $\Delta E_v = E_v|_{\mathrm{an}} - E_v|_{x_{\mathrm{max}}}$. We further note that the electric field is related to E_c and E_v as

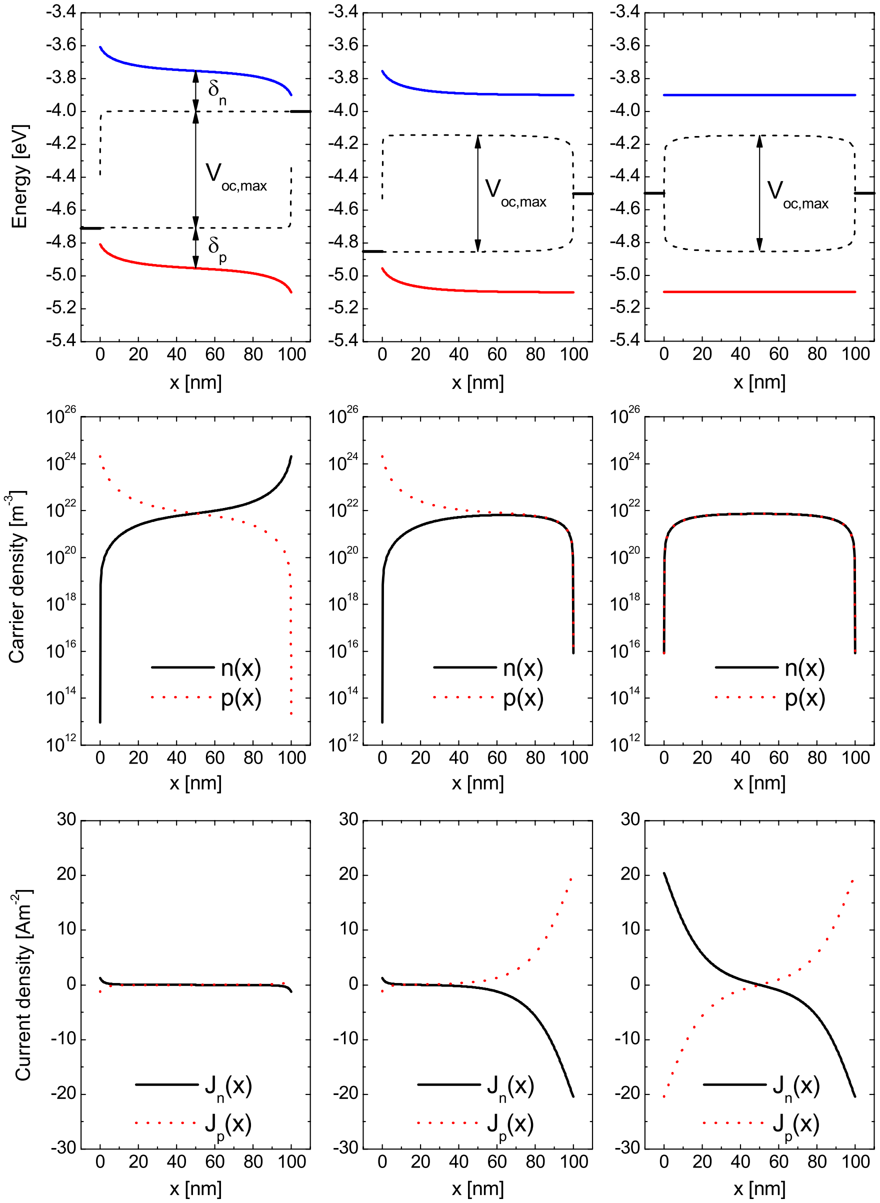

(a) (b) (c)

FIG. 10. Simulated band diagrams (upper panels), carrier densities (middle panels), and carrier current densities (lower panels) for, otherwise, ideal devices at open-circuit conditions (under illumination) but with the injection barriers: (a) $\varphi_{\mathrm{an}} = \varphi_{\mathrm{cat}} = 0.10$ eV, (b) $\varphi_{\mathrm{an}} = 0.10$ eV and $\varphi_{\mathrm{cat}} = 0.60$ eV, and (c) $\varphi_{\mathrm{an}} = \varphi_{\mathrm{cat}} = 0.60$ eV. The corresponding output open-circuit voltages given by the difference between the electron quasi-Fermi level at the cathode ($x = d$) and the hole quasi-Fermi level at the anode ($x = 0$) are $V_{\mathrm{oc}} = V_{\mathrm{oc,max}}$ (a), $V_{\mathrm{oc}} = \frac{1}{2}V_{\mathrm{oc,max}}$ (b), and $V_{\mathrm{oc}} = 0$ (c), where $V_{\mathrm{oc,max}} \approx 0.71$ V. The quasi-Fermi levels are depicted by the thin dashed lines in the upper panel. The input parameters are given in Table I.

$$F = \frac{1}{q}\frac{dE_c}{dx} = \frac{1}{q}\frac{dE_v}{dx}, \tag{A5}$$

and that Eqs. (2) and (3) can be rewritten as

$$J_n = \mu_n n \frac{dE_{Fn}}{dx}, \tag{A6}$$

$$J_p = \mu_p p \frac{dE_{Fp}}{dx}. \tag{A7}$$

At open-circuit conditions, the total steady-state current $J = J_n + J_p$ is zero at every point in the device. This condition is fulfilled either when $J_n = J_p = 0$ or $J_n = -J_p \neq 0$. Consider the following two cases for electrons in the region $x_{\max} \leq x \leq d$:

(i) $\varphi_{\text{cat}} < \delta_n$. In this case, $n_{\text{cat}} > n_{\text{ph}}$, where n_{ph} is the photogenerated electron density. On applying a positive voltage ($V \leq V_{\text{bi}}$), a large number of dark carriers diffuse from the cathode into the device. Open-circuit conditions are reached ($V_{\text{oc}} \leq V_{\text{bi}}$) when the drift current consisting of the photogenerated electrons is canceled by the large diffusion current of dark electrons from the cathode so that $J_n \approx 0$. But according to Eq. (A6), this corresponds to $E_{Fn} \approx$ constant [see Fig. 10(a)] and, consequently, $\Delta E_{Fn} = 0$.

(ii) $\varphi_{\text{cat}} > \delta_n$. In this case, $n_{\text{ph}} > n_{\text{cat}}$ [see Figs. 10(b) and 10(c)]. Consequently, the diffusion current from the cathode ($V \leq V_{\text{bi}}$) is not sufficient to cancel the field-driven photocurrent. In contrast, the open-circuit conditions are reached when the magnitude of the electric field is reduced to such an extent that $F \approx 0$ and the electron current at the cathode becomes driven by diffusion. This current is, correspondingly, canceled by an equal but opposite diffusion current of photogenerated holes, such that $J_n \approx -J_p \neq 0$. According to Eq. (A5), this corresponds to $\Delta E_c \approx 0$ and we obtain $\Delta E_{Fn} = \varphi_{\text{cat}} - \delta_n$.

The two different cases, thus, read

$$\Delta E_{Fn} = \begin{cases} 0 & \text{if } \varphi_{\text{cat}} < \delta_n, \\ \varphi_{\text{cat}} - \delta_n & \text{if } \varphi_{\text{cat}} > \delta_n. \end{cases} \tag{A8}$$

A completely analogous treatment for holes (when $0 \leq x \leq x_{\max}$) gives

$$\Delta E_{Fp} = \begin{cases} 0 & \text{if } \varphi_{an} < \delta_p, \\ \varphi_{an} - \delta_p & \text{if } \varphi_{an} > \delta_p. \end{cases} \tag{A9}$$

Combining Eqs. (A8) and (A9) with Eqs. (11) and (A2), the open-circuit voltage is summarized in the following form:

$$qV_{\text{oc}} = E_g^{\text{DA}} - \max(\varphi_{\text{an}}, \delta_p) - \max(\varphi_{\text{cat}}, \delta_n). \tag{A10}$$

APPENDIX B: SIMULATED ENERGY LEVELS, CARRIER DENSITIES, AND CURRENTS AT OPEN-CIRCUIT IN IDEAL DEVICES

The spatial distributions of the band diagrams, current densities, as well as the carrier densities in the active layer at open-circuit conditions for three different cases are simulated in Fig. 10. The simulations are in excellent agreement with the analytical expressions found in Appendix A. Note that in the case of $\varphi_{\text{cat(an)}} < \delta_{n(p)}$, a small deviation from $J_n = J_p = 0$ is seen at the cathode (anode). This is due to the diffusion of minority carriers being extracted at the wrong electrode. This current is compensated by an equal diffusion of majority carriers (such that $J_n = -J_p$).

APPENDIX C: NUMERICAL METHODS

The coupled equations given in Sec. II are discretized and decoupled using an iterative scheme by Scharfetter and Gummel as outlined in Ref. [55]. This numerical approach was used previously by several other groups [12,24,36]. The resulting tridiagonal system of decoupled equations are implemented using the programming language C and solved iteratively using the routine *tridag* from Ref. [56].

[1] M. A. Green, K. Emery, Y. Hoshikawa, W. Warta, and E. D. Dunlop, Solar cell efficiency tables (version 43), Prog. Photovoltaics **22**, 1 (2014).

[2] G. Li, R. Zhu, and Y. Yang, Polymer solar cells, Nat. Photonics **6**, 153 (2012).

[3] C. Deibel and V. Dyakonov, Polymer-fullerene bulk heterojunction solar cells, Rep. Prog. Phys. **73**, 096401 (2010).

[4] J. Nelson, Polymer:fullerene bulk heterojunction solar cells, Mater. Today **14**, 462 (2011).

[5] M. Jø rgensen, K. Norrman, S. A. Gevorgyan, T. Tromholt, B. Andreasen, and F. C. Krebs, Stability of polymer solar cells, Adv. Mater. **24**, 580 (2012).

[6] N. Grossiord, J. M. Kroon, R. Andriessen, and P. W. M. Blom, Degradation mechanisms in organic photovoltaic devices, Org. Electron. **13**, 432 (2012).

[7] P. W. M. Blom, V. D. Mihailetchi, L. J. A. Koster, and D. E. Markov, Device physics of polymer:fullerene bulk heterojunction solar cells, Adv. Mater. **19**, 1551 (2007).

[8] M. R. Lilliedal, A. J. Medford, M. V. Madsen, K. Norrman, and F. C. Krebs, The effect of post-processing treatments on inflection points in current-voltage curves of roll-to-roll processed polymer photovoltaics, Solar Energy Mater. Sol. Cells **94**, 2018 (2010).

[9] W. R. Mateker, J. D. Douglas, C. Cabanetos, I. T. Sachs-Quintana, J. A. Bartelt, E. T. Hoke, A. El Labban, P. M. Beaujuge, J. M. J. Fréchet, and M. D. McGehee, Improving the long-term stability of PBDTTPD polymer solar cells

through material purification aimed at removing organic impurities, Energy Environ. Sci. **6**, 2529 (2013).

[10] B. T. de Villers, C. J. Tassone, S. H. Tolbert, and B. J. Schwartz, Improving the reproducibility of P3HT:PCBM solar cells by controlling the PCBM/cathode interface, J. Phys. Chem. C **113**, 18978 (2009).

[11] W. Tress, K. Leo, and M. Riede, Influence of hole-transport layers and donor materials on open-circuit voltage and shape of I-V curves of organic solar cells, Adv. Funct. Mater. **21**, 2140 (2011).

[12] A. Wagenpfahl, D. Rauh, M. Binder, C. Deibel, and V. Dyakonov, S-shaped current-voltage characteristics of organic solar devices, Phys. Rev. B **82**, 115306 (2010).

[13] Y. Zhou, J. W. Shim, C. F. Hernanderz, A. Sharma, K. A. Knauer, A. J. Giordano, S. R. Marder, and B. Kippelen, Direct correlation between work function of indium-tin-oxide electrodes and solar cell performance influenced by ultraviolet irradiation and air exposure, Phys. Chem. Chem. Phys. **14**, 12014 (2012).

[14] W. Yang, Y. Yao, and C.-Q. Wu, Mechanisms of device degradation in organic solar cells: Influence of charge injection at the metal/organic contacts, Org. Electron. **14**, 1992 (2013).

[15] M. Glatthaar, M. Riede, N. Keegan, K. Sylvester-Hvid, B. Zimmermann, M. Niggemann, A. Hinsch, and A. Gombert, Efficiency limiting factors of organic bulk heterojunction solar cells identified by electrical impedance spectroscopy, Solar Energy Mater. Sol. Cells **91**, 390 (2007).

[16] A. Kumar, S. Sista, and Y. Yang, Dipole induced anomalous S-shape I-V curves in polymer solar cells, J. Appl. Phys. **105**, 094512 (2009).

[17] J. C. Wang, X. C. Ren, S. Q. Shi, C. W. Leung, and P. K. Chan, Charge accumulation induced S-shape J-V curves in bilayer heterojunction organic solar cells, Org. Electron. **12**, 880 (2011).

[18] A. Nollau, M. Pfeiffer, T. Fritz, and K. Leo, Controlled n-type doping of a molecular organic semiconductor: Naphthalenetetracarboxylic dianhydride (NTCDA) doped with bis(ethylenedithio)-tetrathiafulvalene (BEDT-TTF), J. Appl. Phys. **87**, 4340 (2000).

[19] B. Maennig, M. Pfeiffer, A. Nollau, X. Zhou, K. Leo, and P. Simon, Controlled p-type doping of polycrystalline and amorphous organic layers: Self-consistent description of conductivity and field-effect mobility by a microscopic percolation model, Phys. Rev. B **64**, 195208 (2001).

[20] A. Veysel Tunc, A. De Sio, D. Riedel, F. Deschler, E. Da Como, J. Parisi, and E. von Hauff, Molecular doping of low-bandgap-polymer:fullerene solar cells: Effects on transport and solar cells, Org. Electron. **13**, 290 (2012).

[21] D. Wang, N. Kopidakis, M. O. Reese, and B. A. Gregg, Treating poly(3-hexylthiophene) with dimethylsulfate improves its photoelectrical properties, Chem. Mater. **20**, 6307 (2008).

[22] B. A. Gregg, Transport in charged defect-rich π-conjugated polymers, J. Phys. Chem. C **113**, 5899 (2009).

[23] R. G. E. Kimber, E. N. Wright, S. E. J. O'Kane, A. B. Walker, and J. C. Blakesley, Mesoscopic kinetic Monte Carlo modeling of organic photovoltaic device characteristics, Phys. Rev. B **86**, 235206 (2012).

[24] L. J. A. Koster, E. C. P. Smits, V. D. Mihailetchi, and P. W. M. Blom, Device model for the operation of polymer/fullerene bulk heterojunction solar cells, Phys. Rev. B **72**, 085205 (2005).

[25] V. D. Mihailetchi , H. Xie, B. de Boer, L. J. A. Koster, and P. W. M. Blom, Charge transport and photocurrent generation in poly(3-hexylthiophene):methanofullerene bulk-heterojunction solar cells, Adv. Funct. Mater. **16**, 699 (2006).

[26] K. Maturová, S. S. van Bavel, M. M. Wienk, R. A. J. Janssen, and M. Kemerink, Description of the morphology dependent charge transport and performance of polymer:fullerene bulk heterojunction solar cells, Adv. Funct. Mater. **21**, 261 (2011).

[27] R. C. I. MacKenzie, T. Kirchartz, G. F. A. Dibb, and J. Nelson, Modeling nongeminate recombination in P3HT:PCBM solar cells, J. Phys. Chem. C **115**, 9806 (2011).

[28] W. Tress, K. Leo, and M. Riede, Dominating recombination mechanisms in organic solar cells based on ZnPc and C60, Appl. Phys. Lett. **102**, 163901 (2013).

[29] D. J. Wehenkel, L. J. A. Koster, M. M. Wienk, and R. A. J. Janssen, Influence of injected charge carriers on photocurrents in polymer solar cells, Phys. Rev. B **85**, 125203 (2012).

[30] A. Petersen, T. Kirchartz, and T. A. Wagner, Charge extraction and photocurrent in organic bulk heterojunction solar cells, Phys. Rev. B **85**, 045208 (2012).

[31] S. Schäfer, A. Petersen, T. A. Wagner, R. Kniprath, D. Lingenfelser, A. Zen, T. Kirchartz, B. Zimmermann, U. Würfel, X. Feng, and T. Mayer, Influence of the indium tin oxide/organic interface on open-circuit voltage, recombination, and cell degradation in organic small-molecule solar cells, Phys. Rev. B **83**, 165311 (2011).

[32] A. Wagenpfahl, C. Deibel, and V. Dyakonov, Organic solar cell efficiencies under the aspect of reduced surface recombination velocities, IEEE J. Sel. Top. Quantum Electron. **16**, 1759 (2010).

[33] W. Tress, S. Corvers, K. Leo, and M. Riede, Investigation of driving forces for charge extraction in organic solar cells: Transient photocurrent measurements on solar cells showing S-shaped current-voltage characteristics, Adv. Energy Mater. **3**, 873 (2013).

[34] W. Tress and O. Inganäs, Simple experimental test to distinguish extraction and injection barriers at the electrodes of (organic) solar cells with S-shaped current-voltage characteristics, Solar Energy Mater. Sol. Cells **117**, 599 (2013).

[35] B. Y. Finck and B. J. Schwartz, Understanding the origin of the S-curve in conjugated polymer/fullerene photovoltaics from drift-diffusion simulations, Appl. Phys. Lett. **103**, 053306 (2013).

[36] V. A. Trukhanov, V. V. Bruevich, and D. Y. Paraschuk, Effect of doping on performance of organic solar cells, Phys. Rev. B **84**, 205318 (2011).

[37] F. F. Stelzl and U. Würfel, Modeling the influence of doping on the performance of bulk heterojunction organic solar cells: One-dimensional effective semiconductor versus two-dimensional donor/acceptor model, Phys. Rev. B **86**, 075315 (2012).

[38] T. Kirchartz, W. Gong, S. A. Hawks, T. Agostinelli, R. C. I. MacKenzie, Y. Yang, and J. Nelson, Sensitivity of the

Mott-Schottky analysis in organic solar cells, J. Phys. Chem. C **116**, 7672 (2012).

[39] V. D. Mihailetchi, P. W. M. Blom, J. C. Hummelen, and M. T. Rispens, Effect of metal electrodes on the performance of polymer:fullerene bulk heterojunction solar cells, J. Appl. Phys. **94**, 6849 (2003).

[40] D. Rauh, A. Wagenpfahl, C. Deibel, and V. Dyakonov, Relation of open circuit voltage to charge carrier density in organic bulk heterojunction solar cells, Appl. Phys. Lett. **98**, 133301 (2011).

[41] J. Widmer, M. Tietze, K. Leo, and M. Riede, Open-circuit voltage and effective gap of organic solar cells, Adv. Funct. Mater. **23**, 5814 (2013).

[42] H. Baessler, Charge transport in disordered organic photoconductors-A Monte-Carlo simulation study, Phys. Status Solidi (b) **175**, 15 (1993).

[43] W. F. Pasveer, J. Cottaar, C. Tanase, R. Coehoorn, P. A. Bobbert, P. W. M. Blom, D. M. de Leeuw, and M. A. J. Michels, Unified description of charge-carrier mobilities in disordered semiconducting polymers, Phys. Rev. Lett. **94**, 206601 (2005).

[44] R. Coehoorn and P. A. Bobbert, Effects of Gaussian disorder on charge-carrier transport and recombination in organic semiconductors, Phys. Status Solidi A **209**, 2354 (2012).

[45] G. A. H. Wetzelaer, L. J. A. Koster, and P. W. M. Blom, Validity of the einstein relation in disordered organic semiconductors, Phys. Rev. Lett. **107**, 066605 (2011).

[46] J. C. Blakesley and N. C. Greenham, Charge transfer at polymer-electrode interfaces: The effect of energetic disorder and thermal injection on band bending and open-circuit voltage, J. Appl. Phys. **106**, 034507 (2009).

[47] L. J. A. Koster, M. Kemerink, M. M. Wienk, K. Maturová, and R. A. J. Janssen, Quantifying bimolecular recombination losses in organic bulk heterojunction solar cells, Adv. Mater. **23**, 1670 (2011).

[48] C. Uhrich, D. Wynands, S. Olthof, M. K. Riede, K. Leo, S. Sonntag, B. Maennig, and M. Pfeiffer, Origin of open circuit voltage in planar and bulk heterojunction organic thin-film photovoltaics depending on doped transport layers, J. Appl. Phys. **104**, 043107 (2008).

[49] W. Tress, K. Leo, and M. Riede, Optimum mobility, contact properties, and open-circuit voltage of organic solar cells: A drift-diffusion simulation study, Phys. Rev. B **85**, 155201 (2012).

[50] K. Vandewal, K. Tvingstedt, A. Gadisa, O. Inganäs, and J. V. Manca, On the origin of the open-circuit voltage of polymer-fullerene solar cells, Nat. Mater. **8**, 904 (2009).

[51] G. Garcia-Belmonte, Temperature dependence of open-circuit voltage in organic solar cells from generation-recombination kinetic balance, Solar Energy Mater. Sol. Cells **94**, 2166 (2010).

[52] S. M. Sze, *Physics of Semiconductor Devices* (Wiley & Sons, New York, 1981).

[53] M. A. Lampert and P. Mark, *Current Injection in Solids* (Academic Press, New York, 1970).

[54] O. J. Sandberg, M. Nyman, and R. Österbacka (unpublished).

[55] S. Selberherr, *Analysis and Simulation of Semiconductor Devices* (Springer-Verlag, Wien, 1984).

[56] W. H. Press, S. A. Teukolsky, W. T. Vetterling, and B. P. Flannery, *Numerical Recipes in C: The Art of Scientific Computing* (Cambridge University Press, Cambridge, England, 1992).